5-9-2008

Correlation Between Luminescent Properties and Local Coordination Environment for Erbium Dopant in Yttrium Oxide Nanotubes

Yuanbing Mao
The University of Texas Rio Grande Valley, yuanbing.mao@utrgv.edu

John Bargar

Michael Toney

Jane P. Chang

Correlation between luminescent properties and local coordination environment for erbium dopant in yttrium oxide nanotubes

Yuanbing Mao,[1] John Bargar,[2] Michael Toney,[2] and Jane P. Chang[1,a]

[1]*Department of Chemical and Biomolecular Engineering, University of California, Los Angeles, California 90095, USA*
[2]*Stanford Synchrotron Radiation Laboratory, Stanford Linear Accelerator Center, Stanford, California 94309, USA*

The local dopant coordination environment and its effect on the photoluminescent (PL) spectral features of erbium-doped yttrium oxide nanotubes (NTs) were probed by synchrotron-based x-ray diffraction (XRD), x-ray absorption near-edge spectroscopy (XANES), and extended x-ray absorption fine structure (EXAFS). XRD, XANES, and EXAFS data demonstrate that single phase solid solutions of $Y_{(2-x)}Er_xO_3$ were formed at $0 \leq x < 0.4$ and $1.2 < x \leq 2$, and the valence state of Er ions in the Y_2O_3 NTs is +3. The x-ray spectroscopic data clearly show that the erbium dopants largely reside in two types of sites in the Y_2O_3 host material, both of which possess a well-defined intermediate-range structure, and that the doping of erbium into Y_2O_3 does not cause a loss in intermediate-range order and crystallinity in the $Er^{3+}:Y_2O_3$ NTs. This well-defined distribution of erbium doping inside the Y_2O_3 matrix correlates well with the observed sharp and well-resolved PL behavior of these $Er^{3+}:Y_2O_3$ NTs at around 1.535 μm. © *2008 American Institute of Physics.* [DOI: 10.1063/1.2912486]

I. INTRODUCTION

Luminescent materials have many practical applications in devices involving the artificial production of light. Fiber-optic amplifiers, lasers, waveguides, x-ray imaging, bioimaging, field emission, and electroluminescent displays are well-known examples.[1,2] To improve luminescent characteristics, such as the luminescent efficiency and resolution of images in lighting and display, extensive research has been carried out on rare-earth (RE) ion doped luminescent materials due to the unique luminescent characteristics of RE dopants and their stability in high vacuum.[3] Lately, luminescent materials with particle dimensions in the nanometer regime have attracted intense research interest since luminescent properties were reported to be dependent on the size and morphology of the crystallites.[4,5] Therefore, our as-synthesized trivalent erbium-doped yttrium oxide ($Er^{3+}:Y_2O_3$) nanotubes[6] (NTs) take advantage of the characteristic optical properties of erbium ions and offer the potential size- and morphology-induced enhancement in luminescent properties, thereby enabling better luminescent materials for advanced luminescent and photonic applications, such as optical amplifiers, lasers, and infrared detectors.[7]

There are a few fundamental issues that need to be solved for advanced luminescent materials with enhanced luminescent characteristics.[1,8] First, the selection of a favorable host material is critical.[1,9] In this work, Y_2O_3 is selected as a favorable host material for erbium ion substitution due to the following reasons: (1) Er_2O_3 and Y_2O_3 have identical cubic bixbyite crystal structures with very similar lattice constants and Y^{3+} and Er^{3+} ions have nearly the same ionic radii; (2) Y_2O_3 is a refractory oxide that has a high melting point

($\sim$2400 °C), a very high thermal conductivity ($\kappa_{Y_2O_3}$ = 27 W/mK), chemical stability, optical isotropicity with a refractive index of 1.91, and low phonon energies (380 cm^{-1}),[4] which translate to lower nonradiative transition rates and, thus, higher quantum efficiencies of their optical transitions. Second, the design of a desirable preparation procedure is crucial, as it determines the charge state of the RE ions and local coordination environments around the dopants.[8,10,11] We used a hydrothermal procedure followed by a dehydration process to prepare the $Er^{3+}:Y_2O_3$ NTs.[6] It is well known that the hydrothermal process is a relatively low-temperature method that is suited for large scale syntheses of many materials and usually provides highly crystalline products. More importantly, as we will demonstrate, this procedure was able to retain the optically active trivalent state of erbium ions from its precursor state.[6] Last but not least, the dopant location and distribution in the host material needs to be precisely controlled. This will eliminate the possibility of forming RE ion clusters and/or irregular distribution of RE ions in different crystallographic sites (i.e., interstitial sites). Doped luminescent materials that satisfy these standards usually have higher photoluminescent (PL) efficiencies and better-resolved PL spectra than those that do not. However, the effect of the local coordination environments on the origins of the PL spectral features in nanosized RE-doped oxide systems has not been quantified.[10,12–15]

It is well known that much of the controversy on PL characteristics has stemmed from irregular distribution, clustering, or phase segregation of the RE dopant ions or unbonded surface dopant ions, which can result in broad PL peaks and a low PL efficiency.[16] Even in systems that appear to be quite pure and highly crystalline, reported PL behaviors widely vary. This variance in PL features is attributed to the

a)Electronic mail: jpchang@ucla.edu.

multitude of synthetic methods used for the production of RE ion doped oxide materials, which can result in differences in the dopant environment and/or structural disorder.[6,10,12,13] Previously, high-resolution transmission electron microscopy (TEM) associated with energy-dispersive x-ray spectroscopy and electron diffraction enabled researchers to determine the structure of the host materials but failed to show exactly where the RE ions reside.[6,8] Therefore, in order to extract more accurate information regarding the local coordination environments and the origins of the PL spectral features from our as-synthesized $Er^{3+}:Y_2O_3$ NTs, it is vital to perform a rigorous structural characterization.

X-ray diffraction (XRD) is widely applied to determine the long-range structure of crystalline materials. In the case of materials with moderate to long-range order, the diffraction patterns contain information about the atomic structure (intensities), strain (peak positions), and the particle size (peak widths). In particular, synchrotron-based XRD offers an exceptional resolution and sensitivity, even on very small/ thin samples. This permits the identification and quantification of trace phases in RE ion doped materials. On the other hand, x-ray absorption spectroscopy (XAS), including x-ray absorption near-edge structure (XANES) and extended x-ray absorption fine structure (EXAFS), is a well-known spectroscopic technique based on the excitation of electrons from an inner level to outer unoccupied states as the result of absorbing x-ray energy.[17,18] It is sensitive to the local structure and to the partial empty density of states. As a consequence, XAS has been extensively used to investigate the local structure in bulk systems and at the surface of materials to yield information on the local electronic structure and the coordination environment around an absorbing atom.[19] In recent years, XAS has also been recognized as a powerful probe for determining the local structure around impurities in nanocrystals because of its sensitivity to the short-range order and atomic species surrounding an absorbing site.[11,20–23] XANES is sensitive to the valence state and coordination polyhedra and EXAFS provides precise information about the average structural parameters of a selected element in a complex material, including neighboring coordination numbers and bond lengths. Therefore, we use a combination of complementary synchrotron-based XRD and XAS techniques to study the structural characteristics of these $Er^{3+}:Y_2O_3$ NTs. This provides insight into the local coordination environments and the origins of the PL spectral features of these nanostructured samples, from the long-range order down to the local environment of the trivalent erbium cations.[9,11,24–26] Although these types of experiments have been previously conducted on bulk, thin film, and nanoparticle systems of some RE ion doped oxide materials, only a few studies using synchrotron-based analysis of RE-doped NT oxides have been reported.[5,12–15]

II. EXPERIMENT

A. Sample preparation

The $Er^{3+}:Y_2O_3$ NTs used in this study were synthesized as previously reported.[6] Specifically, high-purity $Y(NO_3)_3$ and $Er(NO_3)_3$ (a total of 1.5 mmol, with a specifically ad-

justed Y^{3+}/Er^{3+} molar ratio) were dissolved in 4 ml de-ionized H_2O, followed by the dropwise addition of 14 ml of $1-2M$ NaOH solution under stirring. After being stirred for 1 h, the milky colloid solution was transferred into a 23 ml Teflon-lined autoclave and subsequently sealed and heated at 130 °C for 7 h. The resulting reaction solution along with the precipitate was naturally cooled down to room temperature and then centrifuged. The colorless supernatant, which included the reaction by-products, was discarded. The precipitate was washed with de-ionized water several times and then dried at 80 °C overnight. Finally, the obtained powder of $Er^{3+}:Y(OH)_3$ NTs was placed into a ceramic crucible and converted into corresponding powder of $Er^{3+}:Y_2O_3$ NTs by annealing at 500 °C for 3 h in a box furnace. In this study, seven $Er^{3+}:Y_2O_3$ NT samples were prepared with doping levels of 0% (Y_2O_3), 5% ($Y_{1.9}Er_{0.1}O_3$), 10% ($Y_{1.8}Er_{0.2}O_3$), 20% ($Y_{1.6}Er_{0.4}O_3$), 40% ($Y_{1.2}Er_{0.8}O_3$), 60% ($Y_{0.8}Er_{1.2}O_3$), and 100% (Er_2O_3), which are denoted as E0NT, E5NT, E10NT, E20NT, E40NT, E60NT, and E100NT, respectively. Here, "E" and "NT" stand for "erbium" and "nanotube," respectively, while the numbers in between represent the doping levels of erbium ions.

B. Measurements

The room temperature PL properties of the $Er^{3+}:Y_2O_3$ NTs with different doping levels were measured in their powder forms with a 488 nm Ar^+ laser operated at 0.5 W. The InGaAs detector was cooled by using liquid nitrogen. To prepare the PL samples, powders of $Er^{3+}:Y_2O_3$ NTs were added into ethanol, and the mixtures were subsequently sonicated for about 1 min and later were air dried upon deposition onto silicon wafers. Both synchrotron-based XRD and XAS measurements were conducted at the Stanford Synchrotron Radiation Laboratory (SSRL). The XAS and XRD data from commercial cubic phase Er_2O_3 and Y_2O_3 powders (99.99%, from Alfa Aesar and CERAC, Inc., respectively) were also collected as references. Synchrotron-based XRD data were collected in reflection mode on beamline 2-1 by using incident x-ray with a photon energy of 14 keV ($\lambda = 0.886$ Å) from $q=1.9$ to 6.3 Å^{-1}, where q is the scattering vector. The wavelength calibration was determined based on the diffraction pattern of LaB_6. The diffracted beam was analyzed with a Si(111) crystal. The powder samples of both the $Er^{3+}:Y_2O_3$ NTs and the references were pressed into a shallow cavity of a quartz sample holder. The loaded samples were rocked throughout the experiment in the x-ray beam. The XAS measurements of the Er L_{III}-edge and Y K-edge radiation for both the $Er^{3+}:Y_2O_3$ NTs and the references were performed on beamline 11-2. Incident x rays were monochromatized by using a silicon (220) double-crystal monochromator and were detected by using an ionization chamber filled with N_2 gas. XAS spectra were recorded in transmission mode. Harmonic rejection was provided by use of a Rh-coated x-ray mirror. The energy calibration was checked by measuring the spectra of the 0.005 μm thick metal foils.

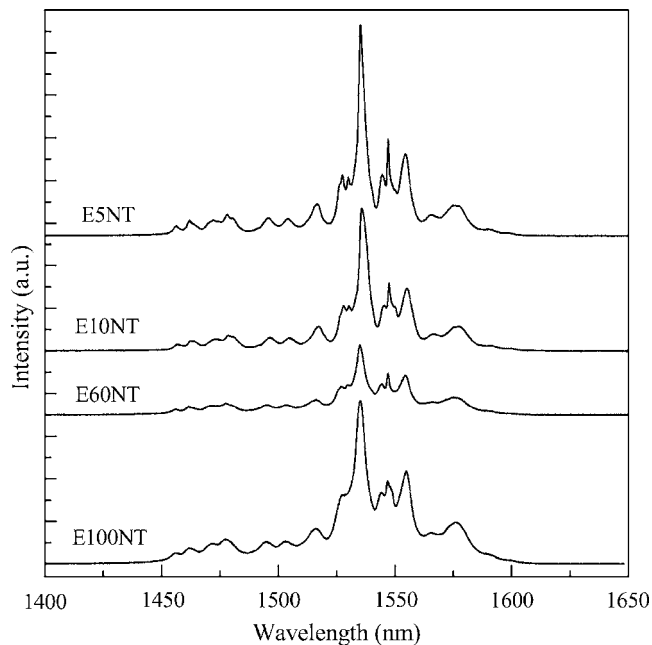FIG. 1. Room temperature PL spectra of the $Er^{3+}:Y_2O_3$ NTs with various doping levels after annealing the as-synthesized $Er^{3+}:Y(OH)_3$ NTs at 500 °C for 3 h (offset for clarification). The intensity variation is likely due to the varying amount of NTs sampled for PL measurements.

FIG. 2. Synchrotron-based XRD patterns of the commercial Y_2O_3 and Er_2O_3 powders and of the $Er^{3+}:Y_2O_3$ NTs with various doping levels after annealing the as-synthesized $Er^{3+}:Y(OH)_3$ NTs at 500 °C for 3 h, which only show the (222) peak to demonstrate the gradual decrease in the *d* value (increase in the *q* value) with an increase in doping levels. The inset shows the (222) and (400) peaks of $Er^{3+}:Y_2O_3$ NTs with various doping levels with a cubic bixbyite structure.

III. RESULTS AND DISCUSSION

A. Photoluminescence

The maximum intensities of the room temperature PL spectra (Fig. 1) were clearly observed at a wavelength of ~ 1.535 μm. These are characteristic of the $^4I_{13/2} \rightarrow {}^4I_{15/2}$ transition of Er^{3+} ions, with full widths at half maximum of only ~ 4 nm. These spectra show similar features with those from the $Er^{3+}:Y_2O_3$ thin film nanostructures prepared by radical-enhanced atomic layer deposition.[9,16,27] The ~ 4 nm full widths at half maximum are much smaller than those of the thin film samples (~ 12 nm).[9,16,27] In general, spectral broadening would be observed if there were an irregular distribution of Er^{3+} on crystallographic lattice sites or some of the Er ions occupied defect sites (i.e., interstitial sites). This would randomize the Stark splitting. In this study, these remarkably sharp and well-resolved PL spectra observed from our as-synthesized $Er^{3+}:Y_2O_3$ NTs at a wavelength of ~ 1.535 μm indicate that erbium cations occupy well-defined locations and retain the optically active trivalent state in the Y_2O_3 lattice, namely, those of Y^{3+} ions, as confirmed by the XRD and XANES analyses discussed in Secs. III B and III C, respectively.

B. XRD

Synchrotron-based XRD is an effective characterization technique for this work since the XRD diffraction pattern of a phase separated binary mixture would show two sets of distinct peaks corresponding to their pure components, while for a solid solution, only one set of diffraction peaks will be present.[26] In this work, XRD patterns from the $Er^{3+}:Y_2O_3$ NTs with different doping levels show that they exhibit only one set of diffraction peaks, which correspond to a cubic

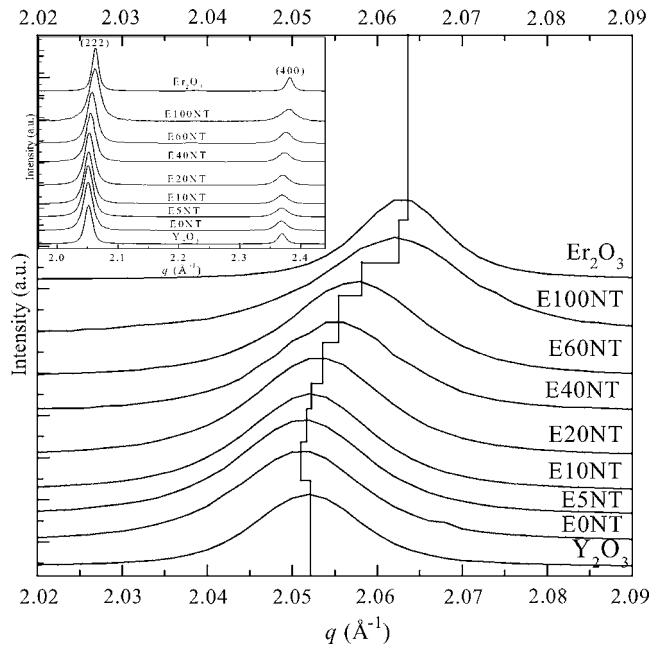bixbyite phase (space group number 206, $Ia3$, Fig. 2). Also, no additional peaks indicating the presence of other phases were found. The diffraction peaks that were indexed match the literature values for Y_2O_3 or Er_2O_3. Therefore, the as-synthesized $Er^{3+}:Y_2O_3$ NTs are pure single phase solid solutions of Y_2O_3 and Er_2O_3.

The XRD patterns exhibit considerable line broadening consistent with the fine-particle nature of the $Er^{3+}:Y_2O_3$ NTs. For the synchrotron-based XRD data from both the as-synthesized $Er^{3+}:Y_2O_3$ NTs and the references, the Bragg peaks were fitted to Pearson-VII functions and the lattice constants were calculated from a least-squares analysis of the Bragg peak positions. The peak broadening was obtained by measuring the width of the strongest diffraction peak (the 222 reflection) because this reflection does not overlap with others. The Scherrer equation was used in calculating crystallite sizes (microstrain was not considered). The calculated lattice constants and crystallite sizes are summarized in Table I. The calculated crystallite sizes are around 30 nm, which are much smaller than the sizes of the $Er^{3+}:Y_2O_3$ NTs observed by scanning electron microscopy (SEM) and TEM. From the SEM and TEM images (Fig. 3), these NTs have lengths in the range of $2-5$ μm, outer diameters of $\sim 100-400$ nm, and inner diameters of 50–100 nm. These indicate that these $Er^{3+}:Y_2O_3$ NTs are polycrystalline. Figure 2 also shows the gradual decrease in the *d* value (corresponding to a gradual decrease in the lattice constant *a*) as a function of Er concentration, as would be expected with the substitution of the smaller Er^{3+} cation (~ 0.89 Å) for the Y^{3+} cation (~ 0.90 Å). For both pure Y_2O_3 and Er_2O_3 NTs, there is a small increase in the lattice constant compared to the

TABLE I. Lattice constants and crystallite sizes obtained from synchrotron XRD studies of the $Er^{3+}:Y_2O_3$ NTs with various doping levels after annealing the as-synthesized $Er^{3+}:Y(OH)_3$ NTs at 500 °C for 3 h as well as those from commercial Y_2O_3 and Er_2O_3 powders.

Sample composition	Lattice constant (Å)	Crystallite size (nm)
Y_2O_3 [a]	10.6041	⋯
Y_2O_3 powder	10.6075	47
Y_2O_3 NTs	10.6122	33
$Y_{1.9}Er_{0.1}O_3$ NTs	10.6106	25
$Y_{1.8}Er_{0.2}O_3$ NTs	10.6070	29
$Y_{1.6}Er_{0.4}O_3$ NTs	10.6019	36
$Y_{1.2}Er_{0.8}O_3$ NTs	10.5910	31
$Y_{0.8}Er_{1.2}O_3$ NTs	10.5792	37
Er_2O_3 NTs	10.5566	25
Er_2O_3 powder	10.5510	53
Er_2O_3 [b]	10.5400	⋯

[a]Reference 36.
[b]Reference 37.

JCPDS information and commercial powders. The commercial powders are micron-sized particles (SEM images not shown), which are composed of nanosized particles, as confirmed by particle size calculation based on the Scherrer equation. This small increase in the lattice constant a for all NT samples is attributed to the fact that they are composed of small particles. Nevertheless, we could not rule out the possible interstitial coordination of Er^{3+} ions from these XRD data. Also, it is possible that the doping induces a localized distortion of the lattice around the dopant. To elucidate the origin, we performed XANES and Er L_{III}-edge EXAFS spectroscopic analyses.

C. XANES

The XANES regions of the x-ray absorption spectrum contain electronic information on the immediate environment of the absorbing atom that, in principle, can be translated into geometrical information. The peak position and the line shape of the spectrum depend on the local electronic structure of the studied ion, providing information on its valence state and site symmetry.[11,14] This information complements that provided by the EXAFS region, which is restricted to interatomic distances. For XANES, data reduction of the XAS measurements were performed with the SIXPACK program by following standard procedures described elsewhere.[9,28] Threshold energy values (at $k=0$), E_0,
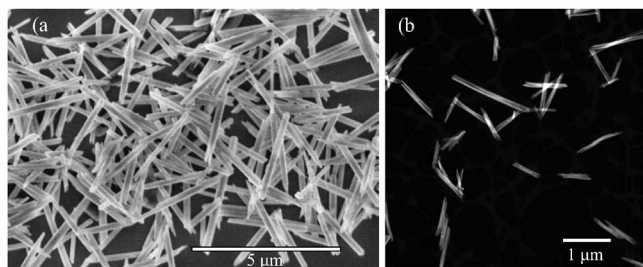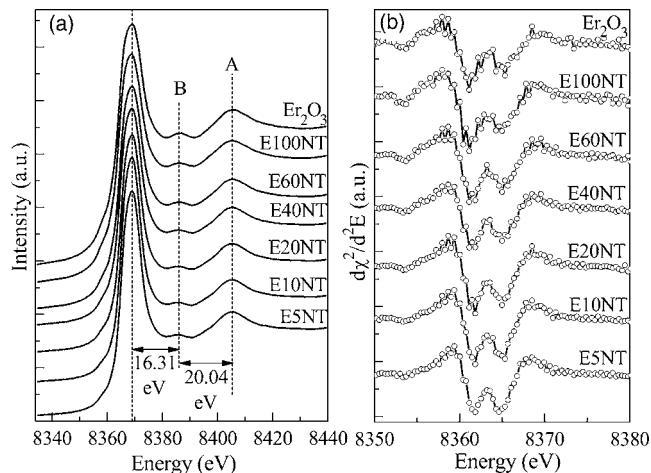

FIG. 4. As-prepared $Er^{3+}:Y_2O_3$ NTs with various doping levels after annealing the as-synthesized $Er^{3+}:Y(OH)_3$ NTs at 500 °C for 3 h and the commercial Er_2O_3 powder: (a) Er L_{III}-edge XANES spectra and (b) second derivatives of the white lines of the Er L_{III}-edge XANES spectra shown in (a). The spectra in both panels were offset for clarification.

were assigned as 8.365 eV for the Er L_{III} edge by using the reference Er_2O_3 powder sample and 17.050 eV for the Y K-edge by using the reference Y_2O_3 powder sample. Figure 4(a) shows the XANES at the Er L_{III} edge for the $Er^{3+}:Y_2O_3$ NTs and commercial Er_2O_3 powder. In Fig. 4(a), the principal x-ray absorption peak appearing at the lower energy side of the Er L_{III} absorption edge is assigned as the "white line," with a pronounced peak at the threshold. The position and intensity of the white line is governed by the electron transition from erbium $2p_{3/2}$ to the erbium $4f5d$ final state and is sensitive to the valence state of the absorbing erbium ions as well as their chemical environment.[19] These peaks from all of the $Er^{3+}:Y_2O_3$ NT and commercial Er_2O_3 powder samples have the same shape and position. Therefore, the valence state of Er ions in the doped Y_2O_3 NTs is +3 and the Er^{3+} ions in the $Er^{3+}:Y_2O_3$ NTs possess a chemical environment similar to those in the commercial Er_2O_3 powder.

For the commercial Er_2O_3 powder, the shape resonance curve exhibits a broad peak (peak A, 36.35 eV higher than the white line) plus a small shoulder peak (peak B, 16.31 eV higher than the white line). The oscillation peak labeled A in Fig. 4(a) is the first EXAFS oscillation and is dominated by Er–O single scattering.[14] Peak B contains single and multiple scattering contributions. Its presence indicates that Er resides in a site possessing a well-defined intermediate-to-long-range structure.[5,8,14,29,30] Thus, the presence of this peak in $Er^{3+}:Y_2O_3$ NT samples indicates well-defined structural order around erbium in these materials, even though a relatively low annealing temperature of 500 °C was applied to the initial $Er^{3+}:Y(OH)_3$ NTs.[8] Specifically, the similarity of both the A and the B peaks from the spectra of these $Er^{3+}:Y(OH)_3$ NTs to that of the commercial Er_2O_3 powder indicates that both materials have a similar local structural environment around Er, with a similar degree of order and are independent of the erbium doping levels.

As shown in Fig. 4(b), the second derivatives of the Er L_{III}-edge XANES spectra for the $Er^{3+}:Y_2O_3$ NTs and the

FIG. 3. (a) SEM and (b) high-angle annular dark field TEM images of the 5% $Er^{3+}:Y_2O_3$ NTs, respectively, after annealing the as-synthesized $Er^{3+}:Y(OH)_3$ NTs at 500 °C for 3 h.
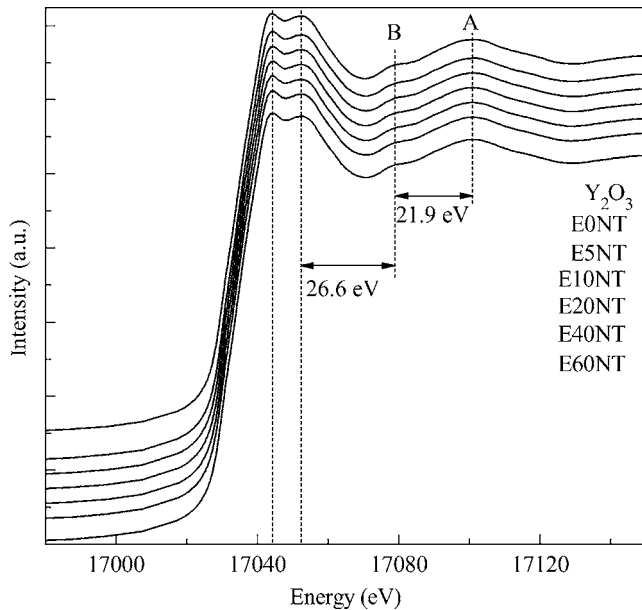
FIG. 5. Y K-edge XANES spectra of the Er^{3+}:Y_2O_3 NTs with various doping levels after annealing the as-synthesized Er^{3+}:$Y(OH)_3$ NTs at 500 °C for 3 h and of the commercial Y_2O_3 powder (offset for clarification).

commercial Er_2O_3 powder were plotted. These data are useful for separating and identifying complex spectra because it highlights the features around the absorbing Er L_{III} edge.[31] They are clearly split into doublets, which indicates that the resonant peaks of Er–O for these Er^{3+}:Y_2O_3 NTs and the commercial Er_2O_3 powder probably originate from two electronic states related to the $4f5d$ orbitals. These data further identified the similarity in terms of the valence state of Er ions, level of structural disorder, and coordination polyhedron between the commercial Er_2O_3 powder and the as-synthesized Er^{3+}:Y_2O_3 NTs.

Figure 5 shows the XANES at the Y K-edge of the Er^{3+}:Y_2O_3 NTs and commercial Y_2O_3 powder. No energy shift is observed in the absorbing Y K edge between the commercial Y_2O_3 powder and the Er^{3+}:Y_2O_3 NTs, which indicates that the Y cations in the Er^{3+}:Y_2O_3 NTs are also trivalent. The double peak structure is due to a splitting of the p orbitals by the distorted octahedral geometry around Y.[32] The oscillation peaks A and B at the higher energy side of the white lines in the XANES spectra at the Y K edge have the same shape and position, which indicates that the levels of structural disorder in these Er^{3+}:Y_2O_3 NTs are similar to the structural disorder level in the commercial cubic phase Y_2O_3 powder.

D. EXAFS and its fitting

The EXAFS spectra were analyzed and modeled by using the standard EXAFS equation and procedure.[5,14,17] In modeling the Er L_{III}-edge EXAFS, theoretical backscattering amplitudes of up to 4 Å radial distance from the center absorbing Er were first calculated by using FEFF 6L.[9] The lattice parameters and the atomic coordinates used for the FEFF calculation were obtained from the crystal structure in the ICSD database.[33,34] Both bulk Er_2O_3 and Y_2O_3 have a cubic bixbyite structure, which belongs to the space group $Ia3 - T_h^7$,

Z=16. The unit cell for this structure consists of 32 metal ions, each coordinated with six O. This bixbyite structure has two nonequivalent symmetry sites available for the metal ions. Specifically, 24 of the 32 metal ions reside in the C_2 symmetry site with the two missing O lying on the face diagonal, resulting in two slightly different metal-oxygen bonds. The remaining eight metal ions are in the C_{3i} symmetry site where the two missing O lie on the body diagonal, yielding six equivalent metal-oxygen bonds. The Er–O bond lengths for the C_2 site are 2.246 and 2.334 Å, whereas that for the C_{3i} sites is 2.263 Å. In our fittings, these differences in the cationic site symmetry (C_2:C_{3i}=3:1) and the Er–O bond length are manifested as a split oxygen shell, with an average coordination of 4.5 O at 2.256 Å and 1.5 O at 2.334 Å. Consequently, the second shell (Er to Er as the second nearest neighbor with a total coordination number of 12) is also a split shell, consisting of six Er^{3+} ions at 3.496 Å and six Er^{3+} ions at 3.985 Å.

Results from the FEFF calculations were used to fit unsmoothed background-subtracted k^3-weighted EXAFS spectra. Quantitative curve fitting were done in the R space over the same R range from 1.0 to 4.5 Å. In addition, the first and second coordination shells were simultaneously used in the fit. Specifically, the following single scattering paths were defined: *First shell.* Er$\leftrightarrow$$O_j$ path described by a bond length $R_{Er\leftrightarrow O_j}$ with a Debye–Waller factor $\sigma_{O_j}^2$. *Second shell.* Er$\leftrightarrow$$M_k$ path at a distance length $D_{Er\leftrightarrow M_k}$ with a Debye–Waller factor $\sigma_{M_k}^2$, where the subscripts j and k denotes O and M at different R and D to the center absorbing Er.[9] In this case, two single scattering paths (j=1 and 2) at 2.26 and 2.33 Å were used to describe the first split O shell. Due to their similar coordination environments and a small difference in bond lengths (within 0.07 Å), only one Debye–Waller factor was used for the first shell ($\sigma_{O_1}^2 = \sigma_{O_2}^2 = \sigma_O^2$). Interactions with the second shell were also described by two scattering paths, each initially set at $D_{Er\leftrightarrow M1}$=3.50 Å and $D_{Er\leftrightarrow M2}$=3.99 Å with Debye–Waller factors of σ_{M1}^2 and σ_{M2}^2, respectively. The structural parameters were then allowed to refine by letting R, D, σ_O^2, and $\sigma_{M_k}^2$ adjust until a best fit with the lowest residual value was obtained. The best fits were derived judging from the residual factor R_{res},

$$R_{res} = \sum_i [k^3(\chi_i^{expt} - \chi_i^{calc})]^2,$$

where χ_i^{expt} and χ_i^{calc} are the experimental and fitting EXAFS spectra, respectively.

An EXAFS analysis on the commercial Er_2O_3 powder reference was first performed in order to establish a structural reference required for determining the chemical identities, coordination numbers, and bond lengths in the Er^{3+}:Y_2O_3 NTs samples and also to assess the accuracy of FEFF fittings. The EXAFS spectrum of the commercial Er_2O_3 powder reference was analyzed on the basis of the Er_2O_3 crystal structure and the single scattering paths mentioned earlier. As shown in Figs. 6 and 7 (solid line), fairly good fits in terms of the oscillation frequency were obtained with this model for commercial Er_2O_3 powder sample. The extracted bond lengths and coordination numbers for the first
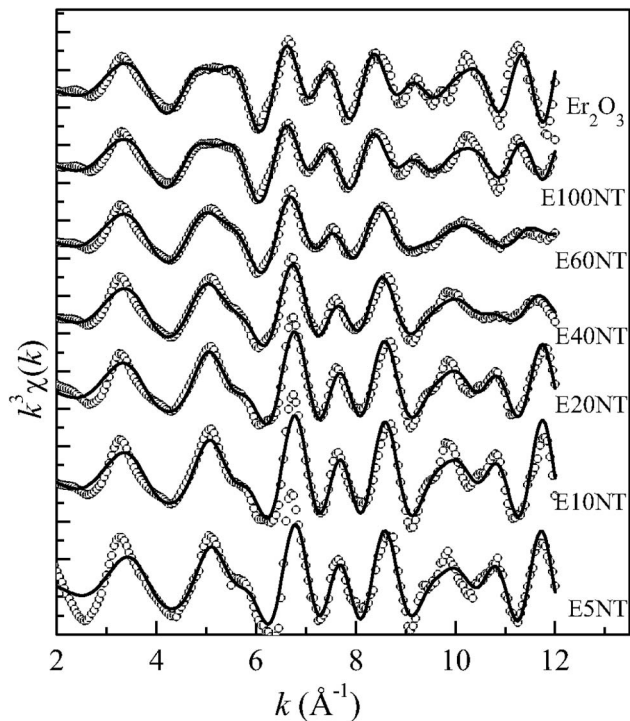
FIG. 6. k^3-weighted Er L_{III}-edge EXAFS (points) and its corresponding fits (lines) of the $Er^{3+}:Y_2O_3$ NTs with various doping levels after annealing the as-synthesized $Er^{3+}:Y(OH)_3$ NTs at 500 °C for 3 h and of the commercial Er_2O_3 powder.
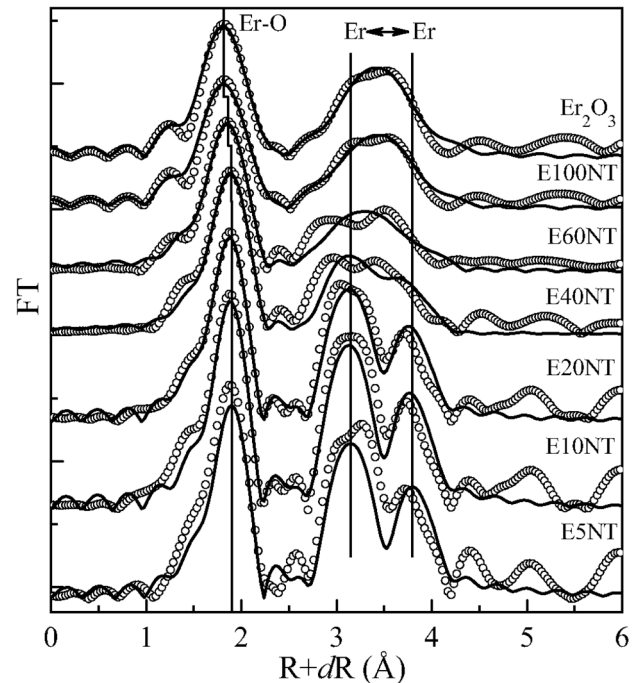

FIG. 7. (Color online) Fourier transformation (points) and corresponding fits (lines) of k^3-weighted Er L_{III}-edge EXAFS of the $Er^{3+}:Y_2O_3$ NTs with various doping levels after annealing the as-synthesized $Er^{3+}:Y(OH)_3$ NTs at 500 °C for 3 h and of the commercial Er_2O_3 powder.

and second shells are in excellent agreement with the reported values (Table II). From these fits, the amplitude reduction factor of Er^{3+} was determined to be 0.91, which is fairly reasonable for heavy elements;[9,16,27] thus, it is set at this value in the subsequent analyses of the $Er^{3+}:Y_2O_3$ NT samples. Moreover, the results show that the multiple scattering signals can be neglected above 4 Å. Therefore, we consider only the single scattering paths in the analysis of the EXAFS spectra of our $Er^{3+}:Y_2O_3$ NT samples.

For all of the $Er^{3+}:Y_2O_3$ NT samples, the coordination number for each shell was fixed according to the Er_2O_3 crystal structural data and the occupancy fraction of all Er in the material comprised by Er atoms having sites with an Er_2O_3 local structure was fixed to unity.[9] The interatomic distance and the Debye–Waller factor for each shell and the refined correction of Fermi energy in vacuum e_0 for $Er \leftrightarrow O$ and $Er \leftrightarrow Er(Y)$ were allowed to vary in the fitting procedure. All of the spectra were treated in exactly the same manner, and the validity of the data reduction and fitting procedures was checked against the spectra of the reference Er_2O_3 and Y_2O_3 compounds. The refinements were carried out to minimize the fitting residue factor R_{res}. Figure 6 shows the Er L_{III}-edge EXAFS functions $k^3\chi(k)$ of the $Er^{3+}:Y_2O_3$ NT samples with different doping levels along with the commercial Er_2O_3 powder sample. It is obvious that for the Er L_{III} edge, the NT spectra are generally similar to one another and slightly differ from those of the commercial Er_2O_3 powder reference. This observation suggests that Er^{3+} ions enter the lattice of Y_2O_3 to substitute at Y^{3+} sites instead of forming Er_2O_3 clusters or nanocrystalline domains that are exsolved within

the host Y_2O_3 phase. These features can be more readily observed in their Fourier transformations (FTs), which are shown in Fig. 7. All distances given in the discussion refer to actual interatomic distances (in angstroms). The corresponding FT peaks include a pair-dependent phase shift. FT peak positions are thus stated in terms of their phase-shifted distance, $R+dR$(Å).

As shown in Fig. 7, the average position of the peak around 1.90 Å, $R+dR$, for each $Er^{3+}:Y_2O_3$ NT sample appears similar to that of the commercial Er_2O_3 powder reference, for which the first atomic polyhedron consists of six oxygen neighbors at average values of 2.26 Å (4.5 O) and 2.33 Å (1.5 O). This peak position shifts upward very slightly with the increase in Y content of the $Er^{3+}:Y_2O_3$ NT samples. This observation enables us to conclude that the erbium ions involved in Er–O bonds are present as Er^{3+} cations. The other peaks above 2.50 Å, $R+dR$, correspond to the more distant $Er \leftrightarrow M_k$ cation neighbors at the nearest second shell. The FT of Er_2O_3 NT sample at the Er L_{III} edge is similar to that of the commercial Er_2O_3 powder sample, while the FTs of all other $Er^{3+}:Y_2O_3$ NT samples at the Er L_{III} edge are different from that of the commercial Er_2O_3 powder sample. When the concentration of Y increases (i.e., Er doping level decreases), the broad poorly resolved double FT peak corresponding to $Er \leftrightarrow M_k$ paths more clearly splits into two separate peaks. The ~3 Å ($R+dR$) peak shifts to lower R, consistent with the presence of Y atoms, which have contrasting backscattering phase and amplitude parameters as compared to $Er \leftrightarrow Er$, which is in the second shell of Er. This shift could also indicate a contraction of the interatomic distance. The higher-R peak is attenuated and shifts to

TABLE II. Structural parameters obtained from EXAFS fittings of the $Er^{3+}:Y_2O_3$ NTs with various doping levels after annealing the as-synthesized $Er^{3+}:Y(OH)_3$ NTs at 500 °C for 3 h. Results from fitting of the Er_2O_3 reference powder are also shown to demonstrate the accuracy of the analysis. The standard deviation value for the last significant digit for each individual fit is shown in the parentheses. The EXAFS refinements give information about coordination number (N), bonding distance (R), distance between central element and the second shell element (D), and thermal vibration (Debye–Waller factor, σ^2). e_0 is the refined correction of the Fermi energy in vacuum, as compared to e_0 in SIXPACK. The statistical R_{res} factor is defined in the text and gives an indication of the quality of fit in the k space.

	XRD		Powder	NTs					
				EXAFS fitting results					
Parameter	Y_2O_3 [a]	Er_2O_3 [b]	Er_2O_3	$Y_{1.9}Er_{0.1}O_3$	$Y_{1.8}Er_{0.2}O_3$	$Y_{1.6}Er_{0.4}O_3$	$Y_{1.2}Er_{0.8}O_3$	$Y_{0.8}Er_{1.2}O_3$	Er_2O_3
R_{Er-O}	2.277	2.256	2.24(1)	2.25(1)	2.25(1)	2.25(1)	2.26(1)	2.25(1)	2.25(1)
	2.335	2.334	2.33(1)	2.33(1)	2.33(1)	2.33(1)	2.34(1)	2.33(1)	2.33(1)
σ_O^2	⋯	⋯	0.007(1)	0.004(1)	0.003(1)	0.004(1)	0.005(1)	0.006(1)	0.007(1)
D_{Er-Er1}	⋯	3.496	3.51(1)	3.51(1)	3.50(1)	3.50(1)	3.50(1)	3.50(1)	3.51(2)
σ_{Er1}^2	⋯	⋯	0.005(1)	0.005(1)	0.005(1)	0.006(1)	0.006(1)	0.008(1)	0.007(1)
D_{Er-Y1}	3.518	⋯	⋯	3.53(1)	3.53(1)	3.53(1)	3.52(1)	3.53(1)	⋯
σ_{Y1}^2	⋯	⋯	⋯	0.005(1)	0.005(1)	0.006(1)	0.006(1)	0.008(1)	⋯
D_{Er-Er2}	⋯	3.985	3.98(1)	3.99(1)	3.97(1)	3.98(1)	3.97(2)	3.97(2)	3.98(2)
σ_{Er2}^2	⋯	⋯	0.005(1)	0.005(1)	0.005(1)	0.006(1)	0.006(1)	0.008(1)	0.007(1)
D_{Er-Y2}	4.000	⋯	⋯	4.01(1)	4.00(1)	4.00(1)	4.00(2)	4.00(2)	⋯
σ_{Y2}^2	⋯	⋯	⋯	0.005(1)	0.005(1)	0.006(1)	0.006(1)	0.008(1)	⋯
R_{res} factor	⋯	⋯	0.0354	0.0858	0.0435	0.0300	0.0487	0.0366	0.0474
e_0	⋯	⋯	−7.6384	−4.8469	−6.9333	−7.3589	−6.5447	−7.9344	−7.9513

[a]Reference 34.
[b]Reference 31.

higher R values, also suggesting the presence of Y in the second shell and/or an expanded interatomic distance. Quantitative analysis of these EXAFS spectra was performed by using the model previously described,[9] which apportions the number of second neighbor Er and Y atoms according to the mole fraction of Er/Y, i.e., assuming complete solid solution of Er_2O_3 in Y_2O_3. To further reduce the degrees of freedom in the fit, the 2.33 Å Er–O shell was constrained to be +0.085 Å relative to the 2.25 Å Er–O shell, D_{Er-Y1} was constrained to be +0.025 Å relative to D_{Er-Er1}, and D_{Er-Y2} was constrained to be +0.035 Å relative to D_{Er-Er2} (Table II), based on the structures of Y_2O_3 and Er_2O_3. Reasonable curve-fitting results were obtained, as shown in Figs. 6 and 7 and summarized in Table II. The uncertainties from the fits for each R value are estimated to be ±0.01 and ±0.02 Å for the first and second coordination shells, respectively. With variation in the doping level, the Debye–Waller factors remain almost the same, indicating that the level of disorder in these samples does not change much, which is consistent with our preceding XANES analysis. Similar phenomena were also reported for nanocrystalline $Tb:Y_2O_3$, $Eu:Y_2O_3$, and $Eu:Lu_2O_3$.[12–14]

As can be seen in Fig. 7, the EXAFS model reproduces all major features of the Er K-edge EXAFS spectra and FTs at high and low Er contents. At intermediate Er content (E40NT, E60NT), the apparent splitting of the second shell FT peaks between 3 and 4 Å ($R+dR$) is slightly underpredicted by the EXAFS model. From this behavior, we infer that the speciation of Er in these particular samples is controlled by mechanisms other than or in addition to the formation of solid solutions. This conclusion is not surprising, as complete solid solution between phases tends to be most limited in the middle of the compositional range.

These observations concerning the local dopant coordination environments of the erbium ions in Y_2O_3 host material have important consequences regarding the origins of the observed PL spectral features of the $Er^{3+}:Y_2O_3$ NTs. It was shown for luminescent materials that the crystal structure and local coordination environment, and consequently the electronic structure of materials, have a profound effect on luminescent properties.[9,12,13,24] Experimental studies demonstrated that an irregular distribution and ion immiscibility of RE ions can cause the spectral broadening and low PL efficiency. An irregular distribution of RE ions on lattice sites or occupancy of some Er ions on defect sites randomizes the Stark splitting, while ion immiscibility causes clustering or precipitating of RE ions within domains. These effects result in RE ions losing their luminescent and lasing properties. Especially, for the $Er:SiO_2$ system, it was found that Er^{3+} ions tended to cluster around the limited nonbridging O in the SiO_2 network to screen their electric charge and consequently formed precipitates.[35] In our case, the Er^{3+} ions do not participate in nonradiative quenching clusters if they are sufficiently isolated (i.e., low doping levels in Y_2O_3), or they could be paired (bridge through O), but still be optically active, if two of them are in proximity (i.e., high doping levels in hosting Y_2O_3, or even pure Er_2O_3 NTs). Therefore, we observed remarkably sharp and well-resolved PL spectra from our as-synthesized $Er:Y_2O_3$ NTs. Furthermore, increasing the level of dopant concentration in our $Er^{3+}:Y_2O_3$ NTs produces only a modest structural disorder in the midcomposition range (as indicated by EXAFS). As higher levels of RE cations are doped into the NTs without a significant increase in disorder or defect density, there will likely be a greater number of optically active pairs of RE cations bridged through O. This effect would cause a decrease in the overall

PL efficiency per dopant in the NTs, but the PL spectra are still well resolved due to the regular distribution of Er^{3+} in the Y_2O_3 host material at both C_2 site and C_{3i} site. This is precisely what we have observed in our room temperature PL measurements (Fig. 1).[6]

IV. CONCLUSIONS

Synchrotron-based XRD, XANES, and EXAFS have been used to study the local coordination environment of erbium dopant in erbium-doped yttrium oxide NTs prepared by a hydrothermal method followed a dehydration process. XRD, XANES, and EXAFS results have shown that (1) single phase solid solutions of $Y_{(2−x)}Er_xO_3$ were formed at $x < 0.4$ and $x > 1.2$; (2) the valence state of Er ions in the doped Y_2O_3 NTs is +3, indicating that the synthetic procedure, i.e., a hydrothermal process followed by a dehydration annealing, was able to retain the optically active trivalent state of erbium cation from its precursor state; (3) the erbium dopant resides largely in two types of sites of the Y_2O_3 host, both of which a possess well-defined intermediate-range structure; and (4) the doping of erbium into Y_2O_3 does not cause a loss in intermediate-range order and crystallinity in the $Er^{3+}:Y_2O_3$ NTs. Furthermore, this study allows us to directly compare the local atomic structure of the RE-doped oxide material and its optical properties. These erbium-doped Y_2O_3 NTs exhibit well-resolved and sharp PL peaks at a wavelength of ~ 1.535 μm, which validates the predictions of erbium ions occupying well-defined locations in the Y_2O_3 lattice. As this study establishes a direct correlation between the local atomic structure of the RE ions and the corresponding optical properties, it provides important insight on improving the optical properties of oxide materials in optoelectronic devices by engineering the RE ions' bonding environment and valence. Moreover, this study on $Er^{3+}:Y_2O_3$ NTs would serve as a model system for probing the local dopant coordination environments and their correlation with PL spectral features.

[1]G. Blasse and B. C. Grabmeier, *Luminescent Materials* (Springer-Verlag, Berlin, 1994).
[2]T. Justel, H. Nikol, and C. Ronda, Angew. Chem., Int. Ed. **37**, 3084 (1998).
[3]A. J. Steckl and J. M. Zavada, MRS Bull. **24**, 16, (1999), and references therein.
[4]F. Vetrone, J.-C. Boyer, and J. A. Capobianco, in *Encyclopedia of Nanoscience and Nanotechnology*, edited by H. S. Nalwa (American Scientific Publishers, Stevenson Ranch, CA, 2004), Vol. 10, p. 725.
[5]Z.-G. Wei, L.-D. Sun, X.-C. Jiang, C.-S. Liao, C.-H. Yan, Y. Tao, J. Zhang, T.-D. Hu, and Y.-N. Xie, Chem. Mater. **15**, 3011 (2003).
[6]Y. Mao, J. Huang, R. Ostroumov, K. L. Wang, and J. P. Chang, J. Phys. Chem. C **112**, 2278 (2008).
[7]A. J. Kenyon, Prog. Quantum Electron. **26**, 225 (2002).
[8]C. Mignotte, J. Non-Cryst. Solids **291**, 56 (2001).
[9]T. T. Van, J. R. Bargar, and J. P. Chang, J. Appl. Phys. **100**, 023115 (2006).
[10]Y. Tao, G. Zhao, X. Ju, X. Shao, W. Zhang, and S. Xia, Mater. Lett. **28**, 137 (1996).
[11]M. H. Nilsen, C. Nordhei, A. L. Ramstad, D. G. Nicholson, M. Poliakoff, and A. Cabanas, J. Phys. Chem. C **111**, 6252 (2007).
[12]Z. Qi, C. Shi, W. Zhang, W. Zhang, and T. Hu, Appl. Phys. Lett. **81**, 2857 (2002).
[13]Y. L. Soo, S. W. Huang, Z. H. Ming, Y. H. Kao, G. C. Smith, E. Goldburt, R. Hodel, B. Kulkarni, J. V. D. Veliadis, and R. N. Bhargava, J. Appl. Phys. **83**, 5404 (1998).
[14]Z. Qi, M. Liu, Y. Chen, G. Zhang, M. Xu, C. Shi, W. Zhang, M. Yin, and Y. Xie, J. Phys. Chem. C **111**, 1945 (2007).
[15]Y. L. Soo, S. W. Huang, Y. H. Kao, V. Chhabra, B. Kulkarni, J. V. D. Veliadis, and R. N. Bhargava, Appl. Phys. Lett. **75**, 2464 (1999).
[16]T. T. Van, J. Hoang, R. Ostroumov, K. L. Wang, J. R. Bargar, J. Lu, H.-O. Blom, and J. P. Chang, J. Appl. Phys. **100**, 073512 (2006).
[17]B. K. Teo, *EXAFS: Basic Principles and Data Analysis* (Springer-Verlag, New York, 1986).
[18]F. W. Lytle, J. Synchrotron Radiat. **6**, 123 (1999).
[19]F. de Groot, Chem. Rev. (Washington, D.C.) **101**, 1779 (2001).
[20]B. D. Yuhas, S. Fakra, M. A. Marcus, and P. Yang, Nano Lett. **7**, 905 (2007).
[21]D. Carta, G. Mountjoy, G. Navarra, M. F. Casula, D. Loche, S. Marras, and A. Corrias, J. Phys. Chem. C **111**, 6308 (2007).
[22]S.-J. Hwang and J.-H. Choy, J. Phys. Chem. B **107**, 5791 (2003).
[23]P. Ghosh, K. R. Priolkar, and A. Patra, J. Phys. Chem. C **111**, 571 (2007).
[24]F. d'Acapito, S. Mobilio, P. Bruno, D. Barbier, and J. Philipsen, J. Appl. Phys. **90**, 265 (2001).
[25]W. Li, A. I. Frenkel, J. C. Woicik, C. Ni, and S. I. Shah, Phys. Rev. B **72**, 155315 (2005).
[26]M. Fernandez-Garcia, A. Martinez-Arias, J. C. Hanson, and J. A. Rodriguez, Chem. Rev. (Washington, D.C.) **104**, 4063 (2004).
[27]T. T. Van and J. P. Chang, Appl. Phys. Lett. **87**, 011907 (2005).
[28]S. M. Webb, Phys. Scr., T **T115**, 1011 (2005).
[29]Z. Y. Wu, C. M. Liu, L. Guo, R. Hu, M. I. Abbas, T. D. Hu, and H. B. Xu, J. Phys. Chem. B **109**, 2512 (2005).
[30]X. Chen, Q. Cai, W. Wang, Z. Chen, Z. Wu, Z. Wu, C. Feng, and Q. Li, J. Phys. Chem. C **111**, 4512 (2007).
[31]M. Ishii, S. Komuro, T. Morikawa, Y. Aoyagi, T. Ishikawa, and T. Ueki, Jpn. J. Appl. Phys., Suppl. **38-1**, 191 (1999).
[32]M. Malvestuto, R. Carboni, F. Boscherini, F. D'Acapito, S. Spiga, M. Fanciulli, A. Dimoulas, G. Vellianitis, and G. Mavrou, Phys. Rev. B **71**, 075318 (2005).
[33]M. Mitric, A. Kremenovic, R. Dimitrijevic, and D. Rodic, Solid State Ionics **101**, 495 (1997).
[34]A. Saiki, N. Ishizawa, N. Mizutani, and M. Kato, J. Ceram. Soc. Jpn. **93**, 649 (1985).
[35]K. Arai, H. Namikawa, K. Kumata, and T. Honda, J. Appl. Phys. **59**, 3430 (1986).
[36]JCPDS Card No. 41-1105 (unpublished).
[37]JCPDS Card No. 01-0827 (unpublished).